ACS Catalysis

pubs.acs.org/acscatalysis

Research Article

Spin-State-Dependent Peroxymonosulfate Activation of Single-Atom M−N Moieties via a Radical-Free Pathway

Jie Miao, Yuan Zhu, Junyu Lang, Jingzhen Zhang, Shixian Cheng, Baoxue Zhou, Lizhi Zhang, Pedro J. J. Alvarez, and Mingce Long*

Cite This: *ACS Catal.* 2021, 11, 9569−9577

Read Online

ACCESS | Metrics & More | Article Recommendations | Supporting Information

ABSTRACT: Transition metal catalysts are known to activate persulfate, but the properties that govern the intrinsic activity of these catalysts are still unknown. Here, we developed a series of catalysts with transition metals anchored on carbon nanotubes (denoted M−N−CNTs, where M = Co, Fe, Mn, or Ni) containing single-atom M−N moieties, to activate peroxymonosulfate for the efficient nonradical oxidation of sulfamethoxazole. The spin state of M−N−CNTs strongly determined their catalytic activity. A large effective magnetic moment with a high spin state (e.g., Co−N) favored the overlap of d orbitals with oxygen-containing adsorbates (such as peroxo species) on metal active sites and promoted electron transfer, which facilitated peroxymonosulfate adsorption and enhanced the oxidation capacity of the reactive species. These findings advance the mechanistic understanding of transition metal-mediated persulfate activation and inform the development of efficient spintronic catalysts for environmental applications.

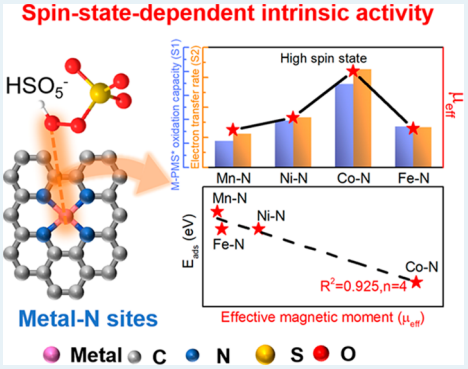

KEYWORDS: *spin state, peroxymonosulfate activation, intrinsic activity, single-atom catalysts, nonradical reaction*

INTRODUCTION

The design of highly active, stable, and cost-effective catalysts for environmental applications is critical for sustainable development.[1,2] The activation of persulfate by heterogeneous catalysts with first-row transition metals has received increased attention due to their efficacy in removing refractory organic pollutants.[3,4] Substantial effort has been devoted to discovering highly active catalysts and understanding the detailed mechanism of persulfate activation.[5−8] Metal centers are the dominant active sites, but different metals show widely different activities in persulfate activation due to unclear reasons. Recently, Mn−O covalency was revealed to have a decisive impact on the intrinsic activity of Co−Mn spinel oxides in peroxymonosulfate (PMS) activation.[5] However, the key properties that govern the intrinsic activity of these catalysts are still unknown, which hinders the rational design of this emerging catalytic advanced oxidation process.

The initial steps of persulfate activation proceed on the metal centers by the adsorption and transformation of persulfate. This is followed by the generation of reactive species, including radicals (e.g., $OH^{\bullet}$ and $SO_4^{\bullet-}$)[9−12] and nonradical species (e.g., singlet oxygen[13] and high-valence metals[14−16]), depending on the chemical environment of the active sites. N-Coordinated metal (M−N) single-atom catalysts (SACs) were demonstrated to effectively mediate persulfate activation on well-defined and atomically dispersed metal active sites.[9−12,15,17] By tuning the bonding structures of metal centers, SACs can activate persulfate through predominantly nonradical pathways that are easier to characterize and control without the confounding effects of free radicals. Accordingly, the almost exclusive conversion of PMS into singlet oxygen was catalyzed by single-atom CoN_{2+2} sites,[18] while high-valence iron (e.g., Fe(V)) species were predominantly formed in some single-atom Fe catalysts.[15,16] Such processes catalyzed by single-atom M−N moieties provide an opportunity to understand the initial steps of persulfate activation on different metal active sites with unprecedented resolution.

Adsorption of persulfate molecules and intermediates and the accompanying electron transfer are the crucial steps of persulfate activation. The adsorbates are mainly oxygen-containing substances.[7,19] Their binding behavior has a direct impact on the oxidation potential of the surface species and electron-transfer rates, which correlate with the catalytic activity in persulfate activation. Recently, the spin state of transition metal catalysts was considered to explain the intrinsic catalytic activities in photocatalytic and electrocatalytic reactions.[20−24] A simple descriptor related to the 3d electronic configuration of transition metals adequately

Received: May 5, 2021
Revised: July 1, 2021
Published: July 16, 2021

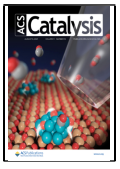

https://doi.org/10.1021/acscatal.1c02031
ACS Catal. 2021, 11, 9569−9577

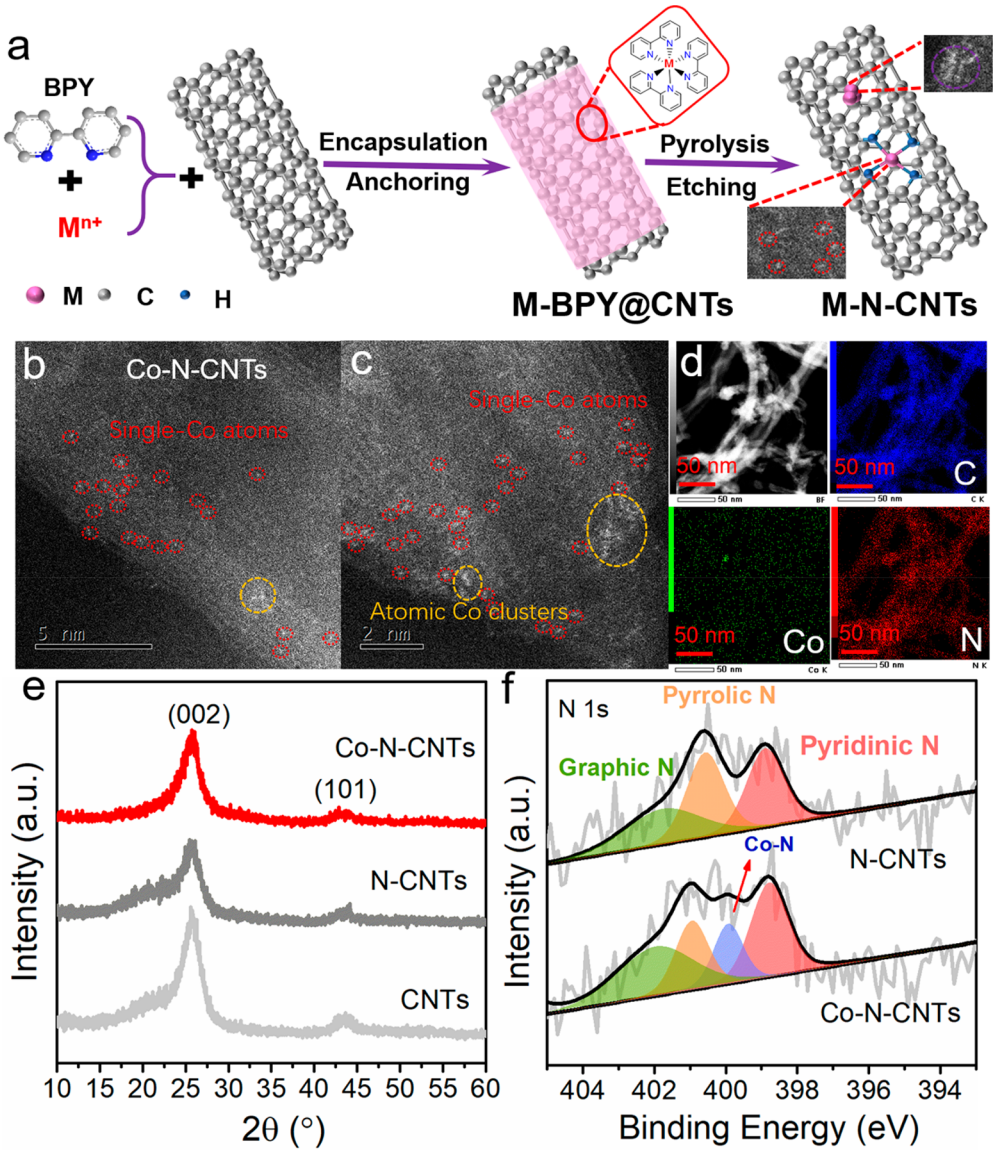

Figure 1. (a) Synthesis process for M−N−CNTs; (b and c) HAADF-STEM images of Co−N−CNTs; (d) EDS images of Co−N−CNTs; (e) XRD patterns of the Co−N−CNT, N-CNT, and CNT catalysts; and (f) N 1s XPS spectra of N-CNT and Co−N−CNT catalysts.

described the interaction between the oxygen-containing species and the active centers in those systems. However, the effect of the spin state on the catalytic activity of M−N moieties for persulfate activation remains unexplored in the literature.

Inspired by the spin state effect on photocatalytic and electrocatalytic systems, and aiming to understand the intrinsic activity of transition metal catalysts in persulfate activation, we developed and tested a series of catalysts with 3d transition metal single-atoms anchored on carbon nanotubes (denoted M−N−CNTs, where M= Co, Fe, Mn, or Ni). Here, we identify the dominant active sites of single-atom M−N moieties; establish correlations between essential indicators of the oxidation potential, electron-transfer rates of surface species, and catalytic activities; and demonstrate the importance of spin states on the intrinsic catalytic activity for persulfate activation via a nonradical mechanism. We discerned the spin state-related catalytic activity in persulfate activation, which informed a new strategy to develop more efficient spintronic catalysts for diverse environmental applications.

RESULTS AND DISCUSSION

Observation of Single-Atom M−N Moieties in Catalysts. The catalysts were synthesized by imbedding M−N (M = Co, Fe, Mn, and Ni) moieties into the framework of carbon nanotubes (CNTs) to provide active sites for PMS activation. The synthesis of M−N−CNT catalysts is illustrated in Figure 1a. The chelate of a metal salt and 2,2-bipyridine (BPY) was first coated on the CNT surface to form M−BPY@CNT precursors. Then, the M−N−CNT catalysts with atomically dispersed M−N_x sites were obtained by calcining M−BPY@CNTs at 800 °C under an Ar atmosphere, followed by acid etching.

The morphologies of the M−BPY@CNTs and the surface M−N moieties were visualized by a high-angle annular dark filed scanning transmission electron microscope (HAADF-STEM). Many bright spots, representing transition metal single atoms,[9,25] were clearly observed on the surfaces of CNTs (Figure 1b and c, Figures S1−S3). Very few clusters can be found, especially for Ni−N−CNTs. No metallic nanoparticles were observed on the M−N−CNT catalysts using a high-

https://doi.org/10.1021/acscatal.1c02031
ACS Catal. 2021, 11, 9569−9577

resolution transmission electron microscope (Figure S4). The results indicate that both single metal atoms and clusters were anchored in the CNT matrix. The coexistence of C, N, and metal elements in M−N−CNTs was demonstrated by the elemental mapping images (Figure 1d and Figure S1b). The contents of the metal elements were determined by inductively coupled plasma mass spectrometry (Table S1). The metal contents in M−N−CNTs were very low and comparable (0.04−0.07 wt %) except for those in Ni−N−CNTs (0.30 wt %), probably because Ni preferred to form clusters that were too robust to be etched by an acid (Figure S3).[26] Figure 1e and Figure S5 show the X-ray diffraction (XRD) patterns of the CNT, N−CNT, and M−N−CNT catalysts. Only two broad peaks were found at 25.8° and 56.1°, which were assigned to the (002) and (101) planes of graphitic carbon, respectively.[27] No peaks of the metal oxides or metallic phases were detected for the M−N−CNT catalysts. In addition, N_2 adsorption and desorption isotherms (Figure S6) and BET specific surface areas (SSAs, Table S1) of the CNT, N−CNT, and all M−N−CNT catalysts were similar. Among them, the SSAs of M−N−CNTs (162.8−178.5 $m^2\ g^{-1}$) were slightly lower than those of N−CNTs (185.4 $m^2\ g^{-1}$) and CNTs (183.2 $m^2\ g^{-1}$), probably due to the slight aggregation of the CNTs.

X-ray photoelectron spectroscopy (XPS) and extended X-ray absorption fine structure spectroscopy (EXAFS) were performed to identify the electronic and coordination structures of M−N_x species in M−N−CNT catalysts. The N 1s XPS spectra of the N−CNT and M−N−CNT catalysts are presented in Figure 1f and Figure S7. The content of N atoms in N−CNTs was 0.28 at % (Table S2), and the N in N−CNTs mainly consisted of pyrrolic N (400.6 eV), graphitic N (401.8 eV), and pyridinic N (398.9 eV).[28] In addition, the embedding of a metal slightly increased the N content to 0.38−0.52 at % in the M−N−CNT catalysts, revealing the formation of the M−N coordination sites. A new peak at approximately 399.9 eV was observed in the N 1s spectra of each M−N−CNT catalyst but not in those of the N−CNTs (Figure 1f and Figure S7), which can be attributed to the M−N species; this suggests the successful formation of M−N coordination sites in M−N−CNTs.[29] The Fourier transform (FT) EXAFS spectrum of the Co *K*-edge of Co−N−CNTs showed peaks at ∼2.17 and ∼1.43 Å, which can be assigned to Co−N and Co−Co scattering paths, respectively (Figure S8a).[9] The Co *K*-edge spectrum of Co−N−CNTs can also be fit well using the two scattering paths (Figure S8b and c and Table S3). This indicates that both Co atomic clusters and single Co atoms exist in Co−N−CNTs, which is consistent with the HAADF-STEM results and XPS analyses.

PMS Activation Was Predominantly Catalyzed by Single-Atom M−N Moieties. The performances of the five M−N−CNT catalysts for PMS activation were assessed by the removal of the recalcitrant sulfonamide antibiotic, sulfamethoxazole (SMX). As shown in Figure 2a, only 49.3% of SMX (initially at 10 mg L^{-1}) was removed within 30 min in the CNTs/PMS systems. In contrast, 100% SMX removal was achieved in 16 min using Co−N−CNTs as the catalyst. During PMS activation, the solution pH varied from 6.8 to 4.9 (Figure S9a), but this pH range had a negligible effect on SMZ degradation rates (Figure S9b). SMX adsorption on all M−N−CNT catalysts was slightly lower than that on CNTs due to the smaller SSAs of the M−N−CNT catalysts (Figure 2c). The other three M−N−CNT catalysts (M = Fe, Mn, and Ni) also exhibited improved performances for SMX removal compared

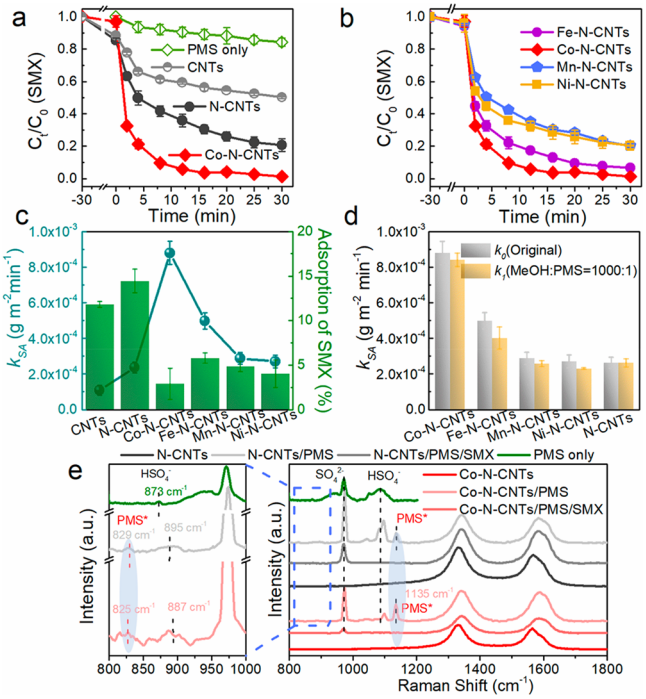

Figure 2. (a and b) SMX degradation in different systems, (c) relationship between the specific activity (k_{SA}) and the adsorption capacity of different catalysts, (d) comparison of SMX oxidation rates in MeOH quenching tests, and (e) in situ Raman spectra of different oxidation systems. Reaction conditions are as follows: $[SMX]_0$ = 10 mg L^{-1}, $[PMS]_0$ = 1.0 mM, [catalyst] = 0.1 g L^{-1}, $[MeOH]_0$ = 1 M, $pH_{initial}$ = 6.8, and T = 25 °C.

to that of pristine CNTs (Figure 2b), indicating that the incorporation of nitrogen-coordinated metal sites resulted in higher activities.

To compare the catalytic performances of these materials, the time-course data were fitted by a pseudo-first-order kinetic model (Figure S10a). Normalizing the observed reaction rate coefficient (k_{obs}) to the SSAs, that is, k_{SA} (g m^{-2} min^{-1}; specific activity), further confirmed the intrinsic activities of all these catalysts (Figure 2c). It shows that the k_{SA} value of Co−N−CNTs (8.80×10^{-4}) was 8.1- and 3.7-fold higher than those of CNTs (1.09×10^{-4}) and N−CNTs (2.37×10^{-4}), respectively. For the different M−N−CNT catalysts (Figure S10b), their k_{SA} values followed the order of Co−N−CNTs > Fe−N−CNTs (4.98×10^{-4}) > Mn−N−CNTs (2.87×10^{-4}) > Ni−N−CNTs (2.70×10^{-4}). Apparently, the incorporated 3d transition metal species (metal clusters or M−N motifs) serve as the main active sites and remarkably boost the catalytic activity of M−N−CNTs.

To ascertain the critical role of metal clusters or single-atom metal sites in M−N−CNT catalysts, the catalysts were treated in a hot acid solution (5 M H_2SO_4) to dissolve and remove the metal clusters. Taking Co−N−CNTs (0.06 wt % Co) and Fe−N−CNTs (0.07 wt % Fe) as the representative M−N−CNT catalysts, the HAAD-STEM images (Figures S1c and S11, respectively) show that most metal clusters were removed, while single metal atoms were still retained on the surface of the catalysts. After treatment, the catalytic activities of Co−N−CNTs (0.01 wt % Co) and Fe−N−CNTs (0.03 wt % Fe) showed negligible differences compared to those of their precursors (Figure S12a and b), demonstrating the dominant role of single metal atoms (M−N moieties) in the catalytic

https://doi.org/10.1021/acscatal.1c02031
ACS Catal. 2021, 11, 9569−9577

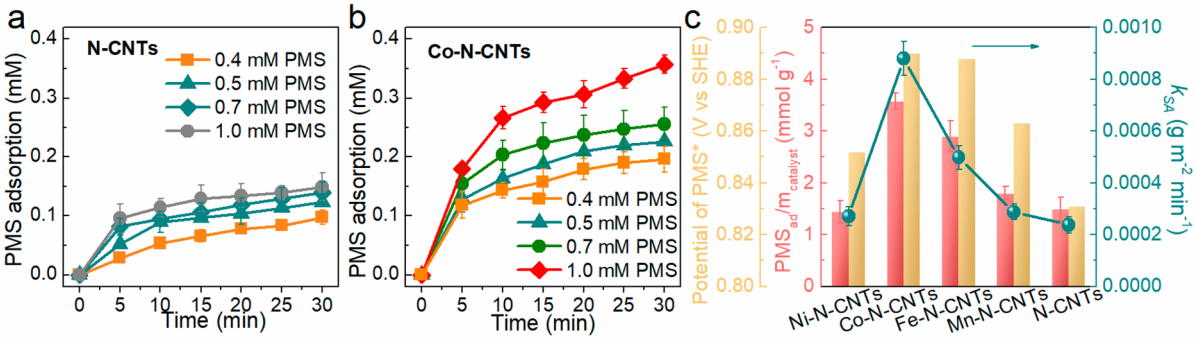

Figure 3. PMS adsorption in (a) N-CNTs/PMS and (b) Co−N−CNT/PMS systems with different PMS doses, and (c) relationship between k_{SA} with $PMS_{ad}/m_{catalyst}$ and the potential of PMS* in different PMS activation systems ($[PMS]_0$ = 1.0 mM). Reaction conditions are as follows: $[SMX]_0$ = 10 mg L^{-1}, [catalyst] = 0.1 g L^{-1}, $pH_{initial}$ = 6.8, and T = 25 °C.

performance of M−N−CNTs. In addition, Co cluster−CNTs (0.1 wt % Co) obtained by the same synthetic procedures but without BPY exhibited a much lower SMX oxidation efficiency than that of Co−N−CNTs (Figure S12c), corroborating the critical role of single metal atoms and the minor contribution of metal clusters.

Nonradical Reactions Predominated in PMS Activation. The involvement of reactive oxygen species (ROS) in the M−N−CNTs/PMS systems was explored by radical quenching, TEMP (2,2,6,6-tetramethyl-4-piperidiny)-trapped electron paramagnetic resonance (EPR), and solvent-exchange tests. Methanol (MeOH) was chosen as the radical scavenger due to its high reactivity with radicals ($SO_4^{\bullet-}$ and $OH^{\bullet}$).[30,31] Figure 2d and Figure S13a and b show no obvious impact on the k_{SA} value with the addition of MeOH (1000 mM), and Figure S13c also presents no EPR signals of hydroxyl or sulfate radicals, indicating the negligible role of free radicals in the N−CNTs/PMS and M−N−CNTs/PMS systems. The EPR signal of TEMP−$^1O_2$ (1:1:1 triplet signals) was observed in both Co−N−CNTs/PMS and N−CNTs/PMS systems (Figure S13d).[32] However, the contribution of $^1O_2$ to SMX degradation is minor due to the negligible difference between the SMX degradation rates in H_2O and D_2O solvents (Figure S13a and b).[4,33] This is consistent with previous reports that $^1O_2$ can be frequently detected in the PMS activation system but contributes a negligible amount to organic degradation.[6,7] We also used DMSO as a probe to detect the presence of high-valence metal-oxo species in M−N−CNTs/PMS systems.[16,34] As shown in Figure S14a, $DMSO_2$ was detected in both the Co−N−CNTs/PMS and PMS-alone systems, and the $DMSO_2$ yield only increased by ∼9% in the presence of the Co−N−CNTs (Figure S14b). This indicates the minor role of the Co-oxo species in the Co−N−CNTs/PMS system. Thus, PMS activation mainly proceeded on the surface of M−N−CNT catalysts via electron transfer in the absence of radicals.

As PMS adsorption onto the catalyst is critical for PMS activation, the initial steps were studied in the absence of SMX. This was accomplished by performing in situ Raman spectroscopy and PMS adsorption and open circuit measurements. In situ Raman spectra were used to understand the adsorption of PMS and the formation of surface complexes. PMS activation can be triggered by attaching a PMS molecule to the catalyst surface to form a metastable and highly reactive peroxo species (labeled PMS*), which can be indicated by the new peaks located at 829 and 1135 cm^{-1} in the Raman spectrum of the catalyst after the addition of PMS (Figure 2e).[7] New peaks emerged in some metal oxides, such as $CuFe_2O_4$[35,36] and $CuO−Co_3O_4$@MnO_2.[37] Taking Co−N−CNTs as a representative type of M−N−CNTs, the new peaks emerging at similar locations in the presence of PMS could be assigned to Co-PMS* due to the predominant role of M−N active sites (Figure 2e). In addition, compared with those in PMS alone, the characteristic peaks of $HO−OSO_3^-$ in the Co−N−CNTs/PMS system showed redshifts (from 873 to 887 cm^{-1} and from 1086 to 1099 cm^{-1}), which were ascribed to the strong interaction between the O−O bond in $HO−OSO_3^-$ and Co−N sites in Co−N−CNTs (Figure 2e). After SMX was added to the Co−N−CNTs/PMS system, the Co-PMS* and $HO−OSO_3^-$ peaks disappeared. These results imply that M−PMS* was the predominant nonradical reactive species that oxidized SMX in the M−N−CNTs/PMS systems, and its performance depended greatly on the interaction between PMS and the M−N moieties.

Figure 3a and b and Figure S15 illustrate that PMS adsorption on N−CNT and M−N−CNT catalysts increased with increasing initial PMS concentrations from 0.4 to 1.0 mM. The specific amounts of PMS adsorbed ($PMS_{ad}/m_{catalyst}$) on different catalysts were determined (Figure S16). For N−CNTs, adsorbed amounts increased slowly with increasing initial PMS concentrations, which was probably due to limited active site availability and the weak interaction with PMS. SMX oxidation was thus insensitive to the increase in PMS doses in the N−CNTs/PMS system (Figure S17a). In contrast, PMS adsorption on M−N−CNT catalysts was significantly enhanced with the increasing PMS concentration, and k_{SA} values steadily increased (Figure S17b−f). This demonstrates that the PMS adsorption capacity was enhanced by the incorporation of metal sites. Furthermore, the $PMS_{ad}/m_{catalyst}$ values of these M−N−CNT catalysts were positively correlated with their k_{SA} values for SMX oxidation as well as with the potentials of the adsorbed reactive species on M−N−CNT catalysts (Figure 3c).

The open-circuit potentials were recorded in situ by a chronopotentiometry method using catalyst electrodes with quantitative PMS addition (Figure S18).[7,32] The initial potentials of all M−N−CNTs were similar (0.02−0.05 V) but increased with different slopes with increasing PMS concentrations, suggesting the generation of a surface-active PMS* species via the oxidation of the M−N−CNT surface by PMS. Compared to those on the N−CNTs, the potentials of PMS* on all the M−N−CNT catalysts were higher at the same PMS dose and grew faster with increasing PMS doses (Figure

https://doi.org/10.1021/acscatal.1c02031
ACS Catal. 2021, 11, 9569−9577

S19), reflecting the stronger oxidation power of the corresponding M−N−CNTs/PMS system and the more efficient electron transfer, respectively. Thus, the larger $PMS_{ad}/m_{catalyst}$ values of M−N−CNT catalysts result in the higher potentials of the PMS* species, leading to enhanced SMX oxidation.

The correlation between $\ln k_{SA}$ and $PMS_{ad}/m_{catalyst}$ or PMS* potentials was determined to assess the intrinsic electron-transfer regime in M−N−CNTs/PMS systems. Figure 4a shows that the value of $PMS_{ad}/m_{catalyst}$ increased linearly with $\ln k_{SA}$ ($R^2 \geq 95.6\%$, $p < 0.05$). Some deviation in linearity for Co−N−CNTs/PMS at $PMS_{ad}/m_{catalyst}$ values greater than 2.56 mmol g^{-1} can be attributed to electron transfer being inhibited on the oxidized CNT surface due to superfluous PMS being adsorbed at high doses.[7] The slope of the fitted linear part was labeled S1, that is, the SMX oxidation rates increased with increased amounts of adsorbed PMS. A higher S1 value represents a faster increase in oxidation rates for the same increased amounts of adsorbed PMS on the catalysts. The S1 values of all M−N−CNTs/PMS systems far exceeded that of N−CNTs/PMS, suggesting that the oxidation performance of the M−N−CNTs/PMS system was better than that of the N−CNTs/PMS, which also depends on the initial PMS concentrations. In addition, the order of the S1 values of M−N−CNTs/PMS systems in Figure 4a is Co−N−CNTs/PMS > Ni−N−CNTs/PMS > Fe−N−CNTs/PMS > Mn−N−CNTs/PMS, which is not consistent with the order of their PMS adsorption capacities. For example, Fe−N−CNTs presented a greater PMS adsorption capacity than Ni−N−CNTs, but when Fe−N−CNTs ($[PMS]_0$ = 0.4 mM) had a $PMS_{ad}/m_{catalyst}$ value (1.44 mmol g^{-1}) similar to that of Ni−N−CNTs ($[PMS]_0$ = 1.0 mM), Ni−PMS* displayed a higher SMX degradation rate ($k_{SA} = 2.70 \times 10^{-4}$ g m^{-2} min^{-1}) than Fe−N−CNTs ($k_{SA} = 2.23 \times 10^{-4}$ g m^{-2} min^{-1}). Thus, S1 can represent the oxidation capacities of the activated species (M−PMS*), which follows the same order as S1. These results suggest that the metal types in the single-atom M−N moieties govern the redox potential of reactive M−PMS* and alter SMX oxidation in the electron-transfer process.

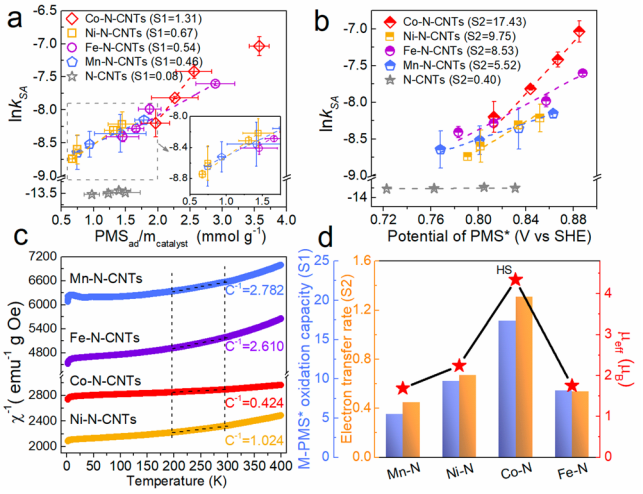

Figure 4. Correlation between $\ln k_{SA}$ and (a) PMS adsorption capacities ($R^2 \geq 95.6\%$, the slope was labeled S1) and (b) the potential of PMS* in different PMS catalytic activation systems ($R^2 \geq 92.7\%$, the slope was labeled as S2). (c) Temperature-dependent inverse susceptibilities fitted by the Curie−Weiss law over different M−N−CNT catalysts (C is the Curie constant, $R^2 \geq 99.4\%$). (d) Correlation between the M−PMS* oxidation capability, the interaction between M−N and PMS, and the effective magnetic moment (μ_{eff}) of the M−N−CNTs catalysts.

The oxidation potential of surface-reactive PMS* at various PMS concentrations was also positively linearly correlated with $\ln k_{SA}$ (Figure 4b), and the slope of the fitted curve was labeled S2. A higher S2 value indicates a faster increase in SMX oxidation rates for a given increase in the M−PMS* oxidation potential. Considering that the M−PMS* potentials represent the oxidation power of the surface species, S2 values directly reflect the electron-transfer rates in PMS activation. The order of the S2 values of the M−N−CNT catalysts was consistent with that of the S1 values. This suggests that the stronger oxidation capacity of M−PMS* has a greater oxidation potential difference with which to promote electron transfer between the adsorbates and organic substrates. Electrochemical impedance spectroscopy (EIS) was conducted to evaluate the electrical conductivity of these catalysts (Figure S20). The order of electrical conductivity for the M−N−CNTs catalysts is consistent with that of S2, corroborating the importance of this value for inferring the electron-transfer ability. Thus, the PMS activation and SMX oxidation performances in the M−N−CNTs/PMS systems depend on the values of S1 (oxidation capacities of PMS*) and S2 (electron-transfer rates), which together represent the intrinsic activity of the catalysts in PMS activation.

Spin-State: A Critical Determinant of Catalytic Activity on Persulfate Activation. The interaction between M−N sites and PMS (M−O−OSO_3H) was further explored by the spin states of the M−N moieties, which were determined by performing temperature-dependent magnetization measurements at H = 1 kOe under field-cooling (ZFC/FC) conditions (Figure S21).[38,39] The susceptibilities that originate from the magnetizations ($\chi = M/H$) abide by the Curie−Weiss law ($\chi = C/(T - \Theta)$), where C is the Curie constant), and the effective magnetic moment ($\mu_{eff} = \sqrt{8C}\mu_B$) can be calculated through the linear fitting of χ^{-1} − T (Figure 4c).[22,40] The μ_{eff} of a 3d transition metal is always derived from the spin splitting of partially occupied d orbitals (e_g and t_{2g}), where μ_{eff} can be calculated by the spin states (S) using the equations $\mu_{eff} = g\mu_B\sqrt{V_{HS}(S_{HS}+1)S_{HS} + V_{LS}(S_{LS}+1)S_{LS}}$ (g = 2) and $V_{HS} + V_{LS} = 1$.[39] The spin states of 3d transition metals in M−N−CNTs are multiples.[24] The possible theoretical μ_{eff} values of all M−N−CNTs at different spin states are listed in Table S4. Figure 4d shows that Co−N−CNTs had the largest experimental μ_{eff} value (4.37 μ_B), followed by Ni−N−CNTs (2.24 μ_B), Fe−N−CNTs (1.75 μ_B), and Mn−N−CNTs (1.69 μ_B). Compared with the theoretical μ_{eff} values in Table S4, the spin states for M−N−CNTs were estimated as S = 2 or 3/2 (Co−N−CNTs), S = 1 (Ni−N−CNTs), S = 1/2 (Fe−N−CNTs), and S = 1/2(Mn−N−CNTs), respectively. The order of the spin states is consistent with that of the μ_{eff} values, that is, a larger μ_{eff} value corresponds to a higher spin state.

The μ_{eff} values of M−N−CNTs were positively correlated with both the S1 and S2 values (Figure 4d), indicating that both the oxidation capacities of M−PMS* and the subsequent electron-transfer rates in PMS activation are governed by the spin states of M−N sites in the catalysts. That is, the larger spin-state values of the M−N−CNTs result in higher catalytic activities for PMS activation. This can be explained by the

https://doi.org/10.1021/acscatal.1c02031
ACS Catal. 2021, 11, 9569−9577

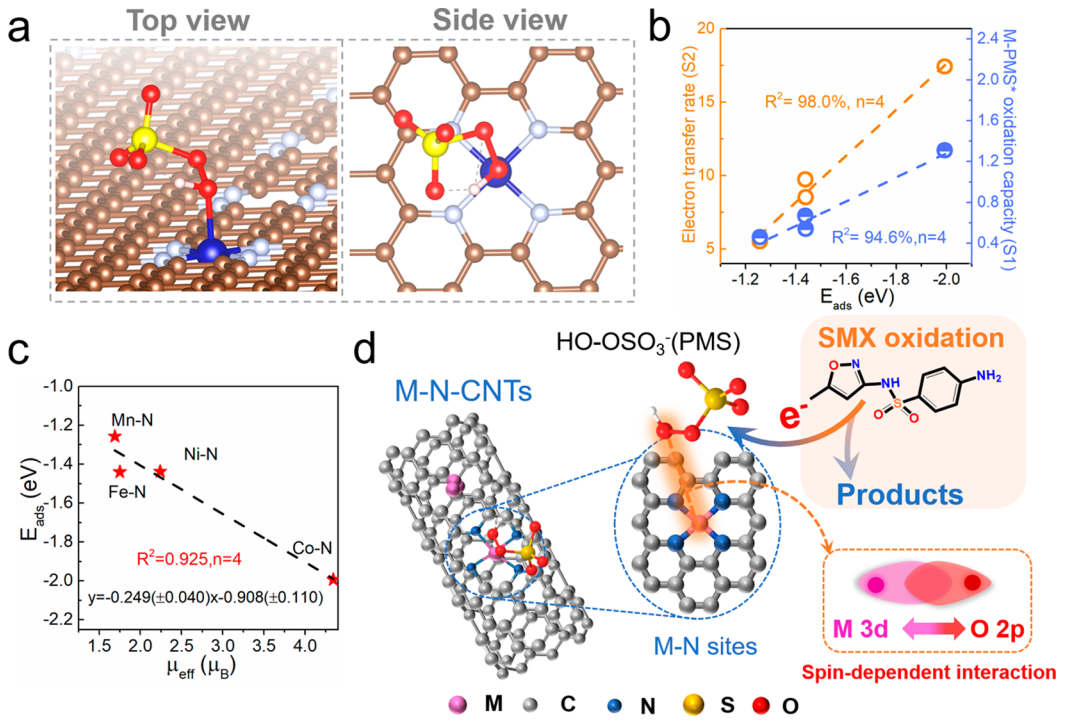

Figure 5. (a) Optimized configurations of PMS adsorbed on Co−N−CNTs, (b) correlation between E_{ads} and the experimental results ($p < 0.05$), (c) correlation between μ_{eff} and E_{ads} ($p < 0.05$), and (d) schematic illustration of the catalytic activation mechanism of M−N−CNTs/PMS.

spatial electronic configurations of the d orbitals in the transition metals. Generally, the e_g orbital of transition metals participates in σ-bonding with oxygen-containing species by overlapping with O 2p orbitals, thus influencing the bonding strength and electron-transfer rates in addition to the catalytic activity for PMS activation.[5,20,41] The high-spin state of M−N sites with a large magnetic moment favors the coupling of oxygen-containing adsorbates on metal sites and enhances the transfer of spin-oriented electrons,[23,24,38,42] thus promoting PMS adsorption, strengthening the oxidation potential of the intermediates, and accelerating electron transfer. This results in better catalytic activity for PMS activation and SMX oxidation.

Density function theory (DFT) calculations were conducted to simulate PMS adsorption on single-atom $M-N_4$ moieties on CNTs. The optimized configurations of PMS adsorbed on different single-atom $M-N_4$ models are shown in Figure 5a and Figure S22. The length of the O−O bond (l_{O-O}) after PMS adsorbed on the catalysts, the adsorption energy (E_{ads}), and the number of electrons transferred (Q) were calculated and are shown in Table 1.[43,44] Compared with free PMS (l_{O-O} = 1.322 Å), adsorbed PMS molecules on the M−N structures have longer O−O bonds, corresponding to PMS activation on the surface metal sites. In addition, l_{O-O} and E_{ads} values followed the order of Co−N > Fe−N > Ni−N > Mn−N. The E_{ads} values showed a high correlation with both the S1 (R^2 = 98.0%, $p < 0.05$) and S2 (R^2 = 96.2%, $p < 0.05$) values, indicating that E_{ads} determines the intrinsic activity for PMS activation on M−N−CNTs (Figure 5b). Co−N showed a lare l_{O-O} value for the adsorbed PMS molecule (1.468 Å) and a better electron-transfer performance (Q = 0.744 e) than those of the other M−N structures. This indicates that the activation of PMS molecules on Co−N moieties is the most effective. The largest PMS adsorption energy (E_{ads} = 1.993 eV) on Co−N moieties indicated that the activated PMS molecules are tightly confined to form surface-reactive PMS complexes rather than to release sulfate radicals (Figure 5a). Previously, a negative linear correlation between the *OH (intermediates in the ORR) adsorption free energy and the magnetic moment of the metal center was reported, indicating the critical role of the magnetic moment on the binding energies of oxygen-related species.[45] Herein, a negative correlation between the E_{ads} and μ_{eff} values was established (R^2 = 0.925, $p < 0.05$) (Figure 5c). This suggests that magnetic moments and spin states may be key factors in modulating the catalytic activity of metal-based catalysts for persulfate activation.

Based on the above analyses, a spin-state-dependent PMS activation mechanism over M−N−CNTs is proposed (Figure 5d). PMS molecules couple with M−N sites to generate surface-reactive complexes, which depend on the spatial configurations of the d orbitals in M−N sites. The interaction between PMS (or oxygen-containing intermediates) and metal sites has spin-state-dependent characteristics. Among these different single-atom M−N sites, Co−N sites with a high-spin state can significantly facilitate PMS adsorption and electron transfer. Thus, the larger the PMS adsorption quantity, the stronger the oxidation potentials of surface reactive M−PMS complexes and the faster the electron-transfer rates that trigger the efficient PMS activation and SMX oxidation via the nonradical electron-transfer process.

Table 1. Summary of DFT Calculation Results for PMS Adsorption on Different M−N−CNT Catalysts

configuration	l_{O-O} (Å)	E_{ads} (eV)	Q (e)
free PMS	1.332		
Co−N (PMS*)	1.468	−1.993	0.744
Fe−N (PMS*)	1.455	−1.440	0.621
Ni−N (PMS*)	1.454	−1.438	0.737
Mn−N (PMS*)	1.434	−1.257	0.485

https://doi.org/10.1021/acscatal.1c02031
ACS Catal. 2021, 11, 9569−9577

CONCLUSION

We fabricated a series of M−N−CNT catalysts for efficient PMS activation by embedding single-atom M−N moieties into the framework of CNTs. The M−N coordination sites were the predominant active sites for PMS adsorption, reactive species generation, and SMX oxidation through a nonradical-dominant pathway. Two significant parameters were found to determine the oxidation capacity of the reactive species and the electron-transfer rates for subsequent SMX oxidation. Both properties are positively correlated with the effective magnetic moment of the materials, suggesting that a high-spin state favors the adsorption of persulfate adsorbates on the metal sites and promotes spin-oriented electron transfer. Thus, a spin-state-dependent mechanism for persulfate activation on single-atom M−N moieties was discerned. These findings highlight the critical role of the spin state of M−N coordination sites in the initial steps of persulfate activation and inform the design of high-performance catalysts for persulfate activation based on spin-state descriptors.

ASSOCIATED CONTENT

Supporting Information

The Supporting Information is available free of charge at https://pubs.acs.org/doi/10.1021/acscatal.1c02031.

Material synthesis, characterization, evaluation of catalytic performance, electrochemical test, theoretical calculations, effects of pH, k_{obs} of SMX oxidation in different PMS systems, quenching tests, GC-MS spectra of DMSO degradation, PMS adsorption in different systems, open-circuit potential curves, PMS* potentials, and spin states and μ_{eff} values of M−N−CNTs (PDF)

AUTHOR INFORMATION

Corresponding Author

Mingce Long − *School of Environmental Science and Engineering, Key Laboratory for Thin Film and Microfabrication of the Ministry of Education, Shanghai Jiao Tong University, Shanghai 200240, China;* orcid.org/0000-0002-5168-8330; Email: long_mc@sjtu.edu.cn

Authors

Jie Miao − *School of Environmental Science and Engineering, Key Laboratory for Thin Film and Microfabrication of the Ministry of Education, Shanghai Jiao Tong University, Shanghai 200240, China*

Yuan Zhu − *School of Environmental Science and Engineering, Key Laboratory for Thin Film and Microfabrication of the Ministry of Education, Shanghai Jiao Tong University, Shanghai 200240, China*

Junyu Lang − *School of Environmental Science and Engineering, Key Laboratory for Thin Film and Microfabrication of the Ministry of Education, Shanghai Jiao Tong University, Shanghai 200240, China*

Jingzhen Zhang − *School of Environmental Science and Engineering, Key Laboratory for Thin Film and Microfabrication of the Ministry of Education, Shanghai Jiao Tong University, Shanghai 200240, China*

Shixian Cheng − *School of Environmental Science and Engineering, Key Laboratory for Thin Film and Microfabrication of the Ministry of Education, Shanghai Jiao Tong University, Shanghai 200240, China*

Baoxue Zhou − *School of Environmental Science and Engineering, Key Laboratory for Thin Film and Microfabrication of the Ministry of Education, Shanghai Jiao Tong University, Shanghai 200240, China;* orcid.org/0000-0001-9691-3119

Lizhi Zhang − *Key Laboratory of Pesticide & Chemical Biology of the Ministry of Education, Institute of Environmental and Applied Chemistry, Central China Normal University, Wuhan 430079, P. R. China;* orcid.org/0000-0002-6842-9167

Pedro J. J. Alvarez − *Department of Civil and Environmental Engineering, Rice University, Houston, Texas 77005, United States;* orcid.org/0000-0002-6725-7199

Complete contact information is available at: https://pubs.acs.org/10.1021/acscatal.1c02031

Notes

The authors declare no competing financial interest.

ACKNOWLEDGMENTS

Financial supports from the National Natural Science Foundation of China (nos. 21876108, 22111530110 and 52070128), the National Key Research and Development Program of China (no. 2017YFE0195800), the NSF ERC on Nanotechnology-Enabled Water Treatment (no. EEC-1449500), and the Shanghai Postdoctoral Excellence Program (no. 2019160) are gratefully acknowledged. We also thank the support in XPS measurements from Mrs. Xue Ding of the Instrumental Analysis Center, Shanghai Jiao Tong University.

REFERENCES

(1) Alvarez, P. J. J.; Chan, C. K.; Elimelech, M.; Halas, N. J.; Villagrán, D. Emerging opportunities for nanotechnology to enhance water security. *Nat. Nanotechnol.* **2018**, *13* (8), 634−641.

(2) Hodges, B. C.; Cates, E. L.; Kim, J. H. Challenges and prospects of advanced oxidation water treatment processes using catalytic nanomaterials. *Nat. Nanotechnol.* **2018**, *13* (8), 642−650.

(3) Kohantorabi, M.; Moussavi, G.; Giannakis, S. A review of the innovations in metal- and carbon-based catalysts explored for heterogeneous peroxymonosulfate (PMS) activation, with focus on radical vs. non-radical degradation pathways of organic contaminants. *Chem. Eng. J.* **2021**, *411*, 127957.

(4) Lee, J.; von Gunten, U.; Kim, J. H. Persulfate-based advanced oxidation: Critical assessment of opportunities and roadblocks. *Environ. Sci. Technol.* **2020**, *54* (6), 3064−3081.

(5) Guo, Z.-Y.; Li, C.-X.; Gao, M.; Han, X.; Zhang, Y. J.; Zhang, W. J.; Li, W. W. Mn-O covalency governs the intrinsic activity of Co-Mn spinel oxides for boosted peroxymonosulfate activation. *Angew. Chem., Int. Ed.* **2021**, *60* (1), 274−280.

(6) Miao, J.; Geng, W.; Alvarez, P. J. J.; Long, M. 2D N-doped porous carbon derived from polydopamine-coated graphitic carbon nitride for efficient nonradical activation of peroxymonosulfate. *Environ. Sci. Technol.* **2020**, *54* (13), 8473−8481.

(7) Ren, W.; Nie, G.; Zhou, P.; Zhang, H.; Duan, X.; Wang, S. The intrinsic nature of persulfate activation and N-doping in carbocatalysis. *Environ. Sci. Technol.* **2020**, *54* (10), 6438−6447.

(8) Yun, E. T.; Lee, J. H.; Kim, J.; Park, H. D.; Lee, J. Identifying the nonradical mechanism in the peroxymonosulfate activation process: Singlet oxygenation versus mediated electron transfer. *Environ. Sci. Technol.* **2018**, *52* (12), 7032−7042.

(9) Li, X.; Huang, X.; Xi, S.; Miao, S.; Ding, J.; Cai, W.; Liu, S.; Yang, X.; Yang, H.; Gao, J.; Wang, J.; Huang, Y.; Zhang, T.; Liu, B. Single cobalt atoms anchored on porous N-doped graphene with dual reaction sites for efficient Fenton-like catalysis. *J. Am. Chem. Soc.* **2018**, *140* (39), 12469−12475.

(10) Xu, H.; Jiang, N.; Wang, D.; Wang, L.; Song, Y.; Chen, Z.; Ma, J.; Zhang, T. Improving PMS oxidation of organic pollutants by single cobalt atom catalyst through hybrid radical and non-radical pathways. *Appl. Catal., B* **2020**, *263*, 118350.
(11) Chu, C.; Yang, J.; Zhou, X.; Huang, D.; Qi, H.; Weon, S.; Li, J.; Elimelech, M.; Wang, A.; Kim, J. H. Cobalt single atoms on tetrapyridomacrocyclic support for efficient peroxymonosulfate activation. *Environ. Sci. Technol.* **2021**, *55* (2), 1242−1250.
(12) Li, H.; Qian, J.; Pan, B. N-coordinated Co containing porous carbon as catalyst with improved dispersity and stability to activate peroxymonosulfate for degradation of organic pollutants. *Chem. Eng. J.* **2021**, *403*, 126395.
(13) Duan, X.; Sun, H.; Shao, Z.; Wang, S. Nonradical reactions in environmental remediation processes: Uncertainty and challenges. *Appl. Catal., B* **2018**, *224*, 973−982.
(14) Li, H.; Shan, C.; Pan, B. Fe(III)-doped g-C_3N_4 mediated peroxymonosulfate activation for selective degradation of phenolic compounds via high-valent iron-oxo species. *Environ. Sci. Technol.* **2018**, *52* (4), 2197−2205.
(15) Jiang, N.; Xu, H.; Wang, L.; Jiang, J.; Zhang, T. Nonradical oxidation of pollutants with single-atom-Fe(III)-activated persulfate: Fe(V) being the possible intermediate oxidant. *Environ. Sci. Technol.* **2020**, *54* (21), 14057−14065.
(16) Qian, K.; Chen, H.; Li, W.; Ao, Z.; Wu, Y. N.; Guan, X. Single-atom Fe catalyst outperforms its homogeneous counterpart for activating peroxymonosulfate to achieve effective degradation of organic contaminants. *Environ. Sci. Technol.* **2021**, *55*, 7034−7043.
(17) Li, Y.; Yang, T.; Qiu, S.; Lin, W.; Yan, J.; Fan, S.; Zhou, Q. Uniform N-coordinated single-atomic iron sites dispersed in porous carbon framework to activate PMS for efficient BPA degradation via high-valent iron-oxo species. *Chem. Eng. J.* **2020**, *389*, 124382.
(18) Mi, X.; Wang, P.; Xu, S.; Su, L.; Zhong, H.; Wang, H.; Li, Y.; Zhan, S. Almost 100% peroxymonosulfate conversion to singlet oxygen on single-atom CoN_{2+2} sites. *Angew. Chem., Int. Ed.* **2021**, *60* (9), 4588−4593.
(19) Duan, X.; Sun, H.; Ao, Z.; Zhou, L.; Wang, G.; Wang, S. Unveiling the active sites of graphene-catalyzed peroxymonosulfate activation. *Carbon* **2016**, *107*, 371−378.
(20) Hwang, J.; Rao, R. R.; Giordano, L.; Katayama, Y.; Yu, Y.; Shao-Horn, Y. Perovskites in catalysis and electrocatalysis. *Science* **2017**, *358* (6364), 751.
(21) Gong, Y.-N.; Zhong, W.; Li, Y.; Qiu, Y.; Zheng, L.; Jiang, J.; Jiang, H. L. Regulating photocatalysis by spin-state manipulation of cobalt in covalent organic frameworks. *J. Am. Chem. Soc.* **2020**, *142* (39), 16723−16731.
(22) Shen, G.; Zhang, R.; Pan, L.; Hou, F.; Zhao, Y.; Shen, Z.; Mi, W.; Shi, C.; Wang, Q.; Zhang, X.; Zou, J.-J. Regulating the spin state of Fe^{III} by atomically anchoring on ultrathin titanium dioxide for efficient oxygen evolution electrocatalysis. *Angew. Chem., Int. Ed.* **2020**, *59* (6), 2313−2317.
(23) Yang, Q.; Jia, Y.; Wei, F.; Zhuang, L.; Yang, D.; Liu, J.; Wang, X.; Lin, S.; Yuan, P.; Yao, X. Understanding the activity of Co-$N_{4-x}C_x$ in atomic metal catalysts for oxygen reduction catalysis. *Angew. Chem., Int. Ed.* **2020**, *59* (15), 6122−6127.
(24) Zhong, W.; Qiu, Y.; Shen, H.; Wang, X.; Yuan, J.; Jia, C.; Bi, S.; Jiang, J. Electronic spin moment as a catalytic descriptor for Fe single-atom catalysts supported on C_2N. *J. Am. Chem. Soc.* **2021**, *143* (11), 4405−4413.
(25) Zhang, X.; Zhang, S.; Yang, Y.; Wang, L.; Mu, Z.; Zhu, H.; Zhu, X.; Xing, H.; Xia, H.; Huang, B.; Li, J.; Guo, S.; Wang, E. A general method for transition metal single atoms anchored on honeycomb-like nitrogen-doped carbon nanosheets. *Adv. Mater.* **2020**, *32* (10), 1906905.
(26) Zhu, Y.; Dai, J.; Zhou, W.; Zhong, Y.; Wang, H.; Shao, Z. Synergistically enhanced hydrogen evolution electrocatalysis by in situ exsolution of metallic nanoparticles on perovskites. *J. Mater. Chem. A* **2018**, *6* (28), 13582−13587.
(27) Chen, P.; Zhou, T.; Xing, L.; Xu, K.; Tong, Y.; Xie, H.; Zhang, L.; Yan, W.; Chu, W.; Wu, C.; Xie, Y. Atomically dispersed iron-nitrogen species as electrocatalysts for bifunctional oxygen evolution and reduction reactions. *Angew. Chem., Int. Ed.* **2017**, *56* (2), 610−614.
(28) Han, A.; Chen, W.; Zhang, S.; Zhang, M.; Han, Y.; Zhang, J.; Ji, S.; Zheng, L.; Wang, Y.; Gu, L.; Chen, C.; Peng, Q.; Wang, D.; Li, Y. A polymer encapsulation strategy to synthesize porous nitrogen-doped carbon-nanosphere-supported metal isolated-single-atomic-site catalysts. *Adv. Mater.* **2018**, *30* (15), 1706508.
(29) Jiao, L.; Wan, G.; Zhang, R.; Zhou, H.; Yu, S.-H.; Jiang, H. L. From metal-organic frameworks to single-atom Fe implanted N-doped porous carbons: Efficient oxygen reduction in both alkaline and acidic media. *Angew. Chem., Int. Ed.* **2018**, *57* (28), 8525−8529.
(30) Hu, P.; Su, H.; Chen, Z.; Yu, C.; Li, Q.; Zhou, B.; Alvarez, P. J. J.; Long, M. Selective degradation of organic pollutants using an efficient metal-free catalyst derived from carbonized polypyrrole via peroxymonosulfate activation. *Environ. Sci. Technol.* **2017**, *51* (19), 11288−11296.
(31) Wei, Y.; Zhang, Y.; Geng, W.; Su, H.; Long, M. Efficient bifunctional piezocatalysis of Au/$BiVO_4$ for simultaneous removal of 4-chlorophenol and Cr(VI) in water. *Appl. Catal., B* **2019**, *259*, 118084.
(32) Du, N.; Liu, Y.; Li, Q.; Miao, W.; Wang, D.; Mao, S. Peroxydisulfate activation by atomically-dispersed Fe-N_x on N-doped carbon: Mechanism of singlet oxygen evolution for nonradical degradation of aqueous contaminants. *Chem. Eng. J.* **2021**, *413*, 127545.
(33) Gao, Y.; Chen, Z.; Zhu, Y.; Li, T.; Hu, C. New insights into the generation of singlet oxygen in the metal-free peroxymonosulfate activation process: Important role of electron-deficient carbon atoms. *Environ. Sci. Technol.* **2020**, *54* (2), 1232−1241.
(34) Li, H.; Shan, C.; Pan, B. Fe(III)-doped g-C_3N_4 mediated peroxymonosulfate activation for selective degradation of phenolic compounds via high-valent iron-oxo species. *Environ. Sci. Technol.* **2018**, *52* (4), 2197−2205.
(35) Zhang, T.; Zhu, H.; Croué, J. P. Production of sulfate radical from peroxymonosulfate induced by a magnetically separable $CuFe_2O_4$ spinel in water: Efficiency, stability, and mechanism. *Environ. Sci. Technol.* **2013**, *47* (6), 2784−2791.
(36) Zhang, T.; Chen, Y.; Wang, Y.; Le Roux, J.; Yang, Y.; Croué, J. P. Efficient peroxydisulfate activation process not relying on sulfate radical generation for water pollutant degradation. *Environ. Sci. Technol.* **2014**, *48* (10), 5868−5875.
(37) Khan, A.; Liao, Z.; Liu, Y.; Jawad, A.; Ifthikar, J.; Chen, Z. Synergistic degradation of phenols using peroxymonosulfate activated by CuO-Co_3O_4@MnO_2 nanocatalyst. *J. Hazard. Mater.* **2017**, *329*, 262−271.
(38) Zhou, S.; Miao, X.; Zhao, X.; Ma, C.; Qiu, Y.; Hu, Z.; Zhao, J.; Shi, L.; Zeng, J. Engineering electrocatalytic activity in nanosized perovskite cobaltite through surface spin-state transition. *Nat. Commun.* **2016**, *7* (1), 11510.
(39) Sun, S.; Shen, G.; Jiang, J.; Mi, W.; Liu, X.; Pan, L.; Zhang, X.; Zou, J. J. Boosting oxygen evolution kinetics by Mn-N-C motifs with tunable spin state for highly efficient solar-driven water splitting. *Adv. Energy Mater.* **2019**, *9* (30), 1901505.
(40) Viciu, L.; Huang, Q.; Morosan, E.; Zandbergen, H. W.; Greenbaum, N. I.; McQueen, T.; Cava, R. J. Structure and basic magnetic properties of the honeycomb lattice compounds $Na_2Co_2TeO_6$ and $Na_3Co_2SbO_6$. *J. Solid State Chem.* **2007**, *180* (3), 1060−1067.
(41) Zhang, T.; Lowry, G. V.; Capiro, N. L.; Chen, J.; Chen, W.; Chen, Y.; Dionysiou, D. D.; Elliott, D. W.; Ghoshal, S.; Hofmann, T.; Hsu-Kim, H.; Hughes, J.; Jiang, C.; Jiang, G.; Jing, C.; Kavanaugh, M.; Li, Q.; Liu, S.; Ma, J.; Pan, B.; Phenrat, T.; Qu, X.; Quan, X.; Saleh, N.; Vikesland, P. J.; Wang, Q.; Westerhoff, P.; Wong, M. S.; Xia, T.; Xing, B.; Yan, B.; Zhang, L.; Zhou, D.; Alvarez, P. J. J. In situ remediation of subsurface contamination: opportunities and challenges for nanotechnology and advanced materials. *Environ. Sci.: Nano* **2019**, *6* (5), 1283−1302.

https://doi.org/10.1021/acscatal.1c02031
ACS Catal. 2021, 11, 9569−9577

(42) Sun, Y.; Sun, S.; Yang, H.; Xi, S.; Gracia, J.; Xu, Z. J. Spin-related electron transfer and orbital interactions in oxygen electrocatalysis. *Adv. Mater.* **2020**, *32* (39), 2003297.
(43) Chen, X.; Duan, X.; Oh, W. D.; Zhang, P. H.; Guan, C. T.; Zhu, Y. A.; Lim, T. T. Insights into nitrogen and boron-co-doped graphene toward high-performance peroxymonosulfate activation: Maneuverable N-B bonding configurations and oxidation pathways. *Appl. Catal., B* **2019**, *253*, 419−432.
(44) Liu, Y.; Luo, J.; Tang, L.; Feng, C.; Wang, J.; Deng, Y.; Liu, H.; Yu, J.; Feng, H.; Wang, J. Origin of the enhanced reusability and electron transfer of the carbon-coated Mn_3O_4 nanocube for persulfate activation. *ACS Catal.* **2020**, *10* (24), 14857−14870.
(45) Xia, D.; Yang, X.; Xie, L.; Wei, Y.; Jiang, W.; Dou, M.; Li, X.; Li, J.; Gan, L.; Kang, F. Direct growth of carbon nanotubes doped with single atomic Fe-N_4 active sites and neighboring graphitic nitrogen for efficient and stable oxygen reduction electrocatalysis. *Adv. Funct. Mater.* **2019**, *29* (49), 1906174.

https://doi.org/10.1021/acscatal.1c02031
ACS Catal. 2021, 11, 9569−9577